

See discussions, stats, and author profiles for this publication at: <https://www.researchgate.net/publication/231646342>

# Ultrafast Laser Ablation and Deposition of Wide Band Gap Semiconductors

ARTICLE *in* THE JOURNAL OF PHYSICAL CHEMISTRY C · FEBRUARY 2011

Impact Factor: 4.77 · DOI: 10.1021/jp108489k

CITATIONS

13

READS

35

10 AUTHORS, INCLUDING:



**Mikel Sanz**

University of Castilla-La Mancha

85 PUBLICATIONS 811 CITATIONS

SEE PROFILE



**Stefano Lettieri**

Italian National Research Council

77 PUBLICATIONS 727 CITATIONS

SEE PROFILE



**Xuan Wang**

Italian National Research Council

169 PUBLICATIONS 2,610 CITATIONS

SEE PROFILE



**Marta Castillejo**

Spanish National Research Council

196 PUBLICATIONS 2,249 CITATIONS

SEE PROFILE

# Ultrafast Laser Ablation and Deposition of Wide Band Gap Semiconductors

Mikel Sanz,<sup>†</sup> Marien López-Arias,<sup>†,‡</sup> José F. Marco,<sup>†</sup> Rebeca de Nalda,<sup>†</sup> Salvatore Amoruso,<sup>§,||</sup> Giovanni Ausanio,<sup>§,||</sup> Stefano Lettieri,<sup>||</sup> Riccardo Bruzzese,<sup>§,||</sup> Xuan Wang,<sup>||</sup> and Marta Castillejo<sup>\*,†</sup>

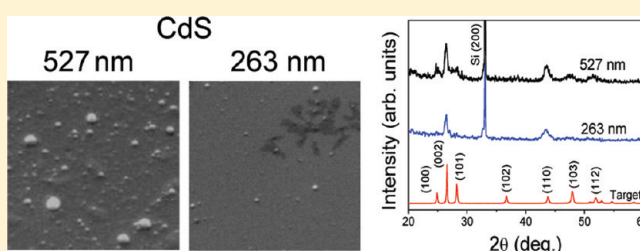
<sup>†</sup>Instituto de Química Física Rocasolano, CSIC, Serrano 119, 28006 Madrid, Spain

<sup>‡</sup>Unidad Asociada Departamento de Química Física I, Facultad de Ciencias Químicas, Universidad Complutense de Madrid, 28040 Madrid, and Instituto de Estructura de la Materia, CSIC, Serrano 123, 28006 Madrid, Spain

<sup>§</sup>Dipartimento di Scienze Fisiche, Università degli Studi di Napoli Federico II, Via Cintia, I-80126 Napoli, Italy

<sup>||</sup>CNR-SPIN, Complesso Universitario di Monte S. Angelo, Via Cintia, I-80126 Napoli, Italy

**ABSTRACT:** Isolated nanoparticles of the wide band gap II–VI semiconductors CdS and ZnS were produced by ultrafast pulsed laser deposition using pulses of  $\approx 300$  fs at two wavelengths of 527 and 263 nm. Upon repetitive target irradiation, the isolated nanoparticles assemble to form a nanostructured film whose structural and chemical properties are compared to those of the targets. UV ablation at 263 nm yields nanoparticles of 5 nm average diameter in the case of CdS. At this wavelength the crystalline phase and stoichiometry of the films markedly differ from those of the target. At 527 nm the average size of the nanoparticles is larger, about 13 nm, but the deposits keep the structural and chemical characteristics of the target. For ZnS the size of the nanoparticles is larger than for CdS although their properties also resemble those of the target when they are produced upon irradiation in the visible. The results obtained allow discussion of the interplay between the light absorption step, the plume dynamics, and the film growth and their impact on the structure and nanometer morphology of the deposited material, while at the same time they exemplify the possibility of their control through the choice of the wavelength of the femtosecond pulses.



## 1. INTRODUCTION

Semiconductor nanoparticles constitute a type of material with broad scientific and technological interest.<sup>1–4</sup> Applications cover the fabrication of novel optoelectronic devices, photonic transducers, and photoluminescent tags for biological studies among others. Methods of synthesis of semiconductor nanoparticles aim at manipulation of electronic properties by controlling size, geometry, and surface characteristics. Pulsed laser deposition (PLD) using ultrashort femtosecond (fs) lasers constitutes a versatile technique with capabilities to adjust laser and deposition parameters in order to fabricate nanoparticles with the required properties. In particular, the variation of laser irradiation conditions can cause neatly distinct ablation processes, with consequences in both the nature of the species initially ejected from the target and the characteristics of the plasma, which can favor varying degrees of aggregation or fragmentation. With ultrashort pulses in the fs regime, the laser intensity on the target is sufficiently high for multiphoton absorption processes to take place, and therefore it is even possible to fabricate by PLD thin films and nanostructures of materials with low optical absorption coefficient at the laser wavelength. Hence, this capability has resulted in the widespread application of fs PLD to a broad variety of materials such as metals, oxides, nitrides, and semiconductors.<sup>5–13</sup>

Despite the rapid increase of studies on fs PLD, progress is still needed to clarify the influence of the ultrashort laser parameters (wavelength, fluence, laser spot size, etc.) on the structure and morphology of deposits and to experimentally test advanced theoretical models.<sup>14,15</sup> In particular, few reports have focused on the wavelength dependence of the characteristic size of deposited nanostructures fabricated by fs PLD.<sup>8–10,12,16,17</sup> For semiconductors, the largest differences could be expected for irradiation at laser wavelengths above or below the band gap, as the order of nonlinear absorption process may substantially differ.

Nanostructures of II–VI semiconductor materials such as CdS and ZnS are attracting expanding interest because they show significant quantum confinement effects which influence their electrical and optical properties.<sup>3,4,18</sup> The possibility to tune the properties of the nanostructures also motivates research into their application in photovoltaic, photonic, and optoelectronic devices and sensors. Nanoparticles and nanostructures of CdS and ZnS have been produced using wet chemistry methods, Langmuir-Blodgett, sputtering, molecular beam epitaxy, and PLD with nanosecond and femtosecond pulses.<sup>1,18–31</sup> In previous

**Received:** September 6, 2010

**Revised:** November 22, 2010

**Published:** February 04, 2011

work,<sup>9</sup> we have shown that laser deposits produced by ablating a CdS target with pulses of 60 fs, focused down to a beam diameter of 50  $\mu\text{m}$ , at three different wavelengths of 266, 400, and 800 nm consist of isolated nanoparticles with average diameters that scale with wavelength. In order to explore further the wavelength effect in fs PLD, in this work, CdS and ZnS nanostructured deposits have been grown on Si(100), glass, and mica substrates by laser ablating CdS and ZnS targets in vacuum using  $\approx 300$  fs laser pulses at 527 and 263 nm. The effect of the laser irradiation wavelength on the sizes of deposited isolated nanoparticles and on the properties of nanoparticle assembled films is investigated. We report on the surface morphology of deposits, their crystalline quality and composition, and their electronic properties, the latter by measuring their UV–vis optical absorption and photoluminescence spectra. It is observed that the size of individual nanoparticles increases with laser wavelength, thus confirming the trend observed previously on CdS with pulses of 60 fs.<sup>9</sup> Furthermore, the structural and chemical properties of the target are transferred to the nanoparticle assembled films when ablation is carried out in the visible, while crystalline phase and stoichiometry change upon ablation in the UV.

## 2. EXPERIMENTAL METHODS

The experimental setup consists of a PLD stainless steel chamber evacuated by a turbomolecular pump (typical background pressure of  $5 \times 10^{-5}$  Pa). The CdS and ZnS targets were prepared from CdS powder (Alfa Aesar 99.999%, particle size  $<44 \mu\text{m}$ ) and ZnS powder (Sigma Aldrich 99.99%, particle size  $<10 \mu\text{m}$ ) that were pelletized into disks of 10 mm diameter and about 2 mm thickness using a hydrostatic press at 8 ton/cm<sup>2</sup> followed by sintering at 350 °C in air for 12 h. The targets were placed on a rotating holder during ablation to avoid cratering. Pulses of  $\approx 300$  fs at 527 nm were produced by compressed second harmonic generation of the fundamental pulse (1054 nm,  $\approx 0.9$  ps) of a Nd:Glass laser system (Light Conversion Twinkle). Pulses of  $\approx 300$  fs at 263 nm were generated by frequency doubling of the visible radiation in a KDP crystal. The laser beam was focused at 45° onto the target surface with a 25 cm focal length lens. The pulse energy was varied with neutral density filters.

The composition and expansion dynamics of the ablation plume were measured by optical emission spectroscopy with temporal and spatial resolution using a system described elsewhere.<sup>32</sup> Briefly, the emitting plasma plume was imaged on the entrance slit of an imaging spectrograph by means of a Nikon lens. The image was registered with an intensified-charge-coupled device (ICCD) camera operated in time-gated detection mode. Spectrally resolved 1D images of the plume were acquired by accumulating the signal over 20 laser shots at a repetition rate of 1 Hz.

Nanoparticle-assembled films on Si(100) and glass substrates placed at 3 cm from the target at room temperature (23 °C) were produced at the visible and UV wavelengths with  $\sim 1.2 \times 10^5$  laser pulses at 33 Hz. Deposits consisting of isolated nanoparticles were also prepared on mica substrates using a lower number of laser pulses up to  $\sim 2.2 \times 10^4$ .

The surface morphology of the deposits was examined by AFM (Digital Instruments Nanoscope IIIa) in tapping mode and by ESEM (Philips XL30). The size distribution of individual nanoparticles was determined by AFM analysis on less-than-one layer deposits onto mica substrates. After deconvolution was

performed on each AFM image, and in order to avoid the tip size effect, the average size of the particles was evaluated with the planes both parallel and orthogonal to the substrate. In this way, the three-dimensional view of the deposited nanoparticle was reconstructed, and its equivalent spherical diameter (ESD) was obtained.<sup>32</sup>

The crystallinity of the deposits was studied by XRD (Philips XPert) using Cu K $\alpha$  (1.54 Å) radiation in the  $\theta/2\theta$  configuration. The stoichiometry of deposits was also analyzed by XPS using a Leybold LHS-10 XPS spectrometer, under an operating vacuum better than  $1 \times 10^{-6}$  Pa, with the Mg K $\alpha$  line (130 W) and analyzer transmission energy of 200 and 20 eV for the wide and narrow scan spectra, respectively. Relative atomic concentrations were calculated using tabulated atomic sensitivity factors.<sup>33</sup>

UV–vis absorption spectra of deposits on glass were recorded using bare glass plates as reference, on a Shimadzu UV-3600 spectrophotometer in the 250–800 nm range. Room temperature photoluminescence spectra of deposits were measured using as excitation source a HeCd laser emitting at 325 nm and a monochromator (320 mm effective focal length, 150 grooves/mm grating) equipped with a thermocoiled CCD camera system. Spectra were recorded with an accumulation time of 3–5 s and corrected by the system spectral response.

## 3. RESULTS AND DISCUSSION

The laser fluence ablation thresholds  $F_{\text{th}}$  and beam radius  $\omega_0$  on the target were determined by the spot regression method,<sup>9</sup> assuming a Gaussian intensity distribution for the focused beam. The beam radii are about 100 and 50  $\mu\text{m}$  at the wavelengths of 527 and 263 nm, respectively. Therefore, under irradiation in the visible, the laser spot area on the target is about  $30 \times 10^{-5} \text{ cm}^2$  and 4 times lower in the UV. The fluence thresholds were not observed to depend noticeably on the wavelength and are typically 300 mJ/cm<sup>2</sup> for CdS and 150 mJ/cm<sup>2</sup> for ZnS. Deposits were prepared with pulse energies in the ranges of 400–800  $\mu\text{J}$  in the visible and of 100–250  $\mu\text{J}$  in the UV resulting in fluences well above the ablation threshold at both wavelengths.

The ablation plume was analyzed by optical emission spectroscopy with spatial and temporal resolution at the ablation conditions established to fabricate deposits. The optical emission observed from the ablation plumes of both CdS and ZnS in all explored conditions consists of intense lines that are assigned to neutral and singly ionized atomic species. Figure 1 displays as an example a spectrally resolved 1D image of the CdS plume at 120 ns delay with respect to the laser pulse onset. For this compound the most prominent emissions are due to Cd I and Cd II. For ZnS, emissions are attributed to Zn I and Zn II. The atomic emission lines are followed at longer delay times by a very dim, structureless continuum, typically observed with high intensity in the fs laser ablation of various types of targets<sup>5,7,12,34,35</sup> and are attributed to emissions from hot nanoparticles produced during the ultrafast ablation process. The lower intensity of the overall emission of the ablated species indicates a less efficient ablation with respect to metallic targets, in similar experimental conditions. Moreover, the comparatively lower intensity of the emission from nanoparticles with respect to the atomic plume also suggests that nanoaggregates are produced with limited excitation energy or lower efficiency during ultrafast laser ablation of the semiconductor materials studied in this work.

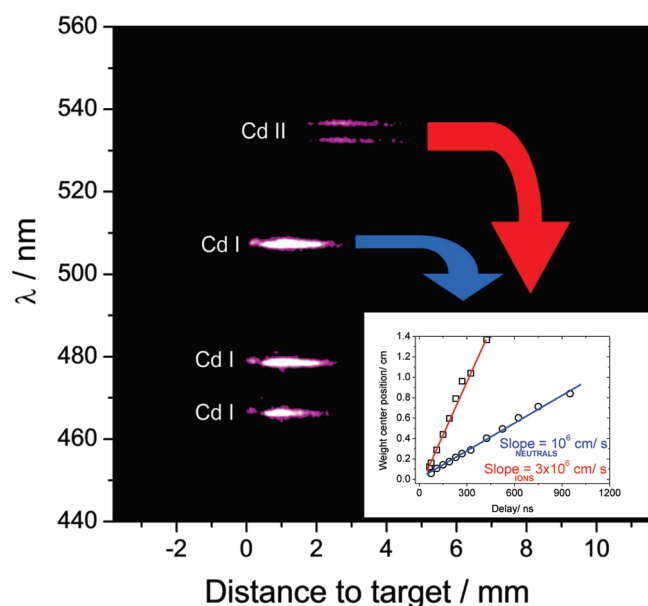


**Figure 1.** Spectrally resolved 1D image of the 527 nm CdS plume acquired at 120 ns delay with respect to the laser pulse onset (pulse energy 440  $\mu$ J). The inset displays the weight center position of the indicated neutral and ionic Cd lines as a function of the delay and the velocities estimated from the linear fit to the data.

Upon ablation at 527 nm, the average expansion velocity of emitting species in the plume reaches  $\approx 10^6$  cm/s and around twice this value at 263 nm. The inset of Figure 1 illustrates the determination of the velocity for two emitting Cd I and Cd II species. The values of expansion velocity are consistent with previous observations on the atomic component typically produced in ultrafast laser ablation of various materials including metals and semiconductors.<sup>5,7,12,34,35</sup> Thus ablation in the UV causes an increase of plasma kinetic energy which in turn has implications for the growth of deposits as will be discussed later.

For a detailed analysis of the nanoparticles and nanostructured films fabricated by fs PLD, AFM images were taken in the deposits consisting of isolated nanoparticles (less-than-one layer deposits) grown on mica with a low number of pulses and also in the nanoparticle-assembled films grown on Si(100) with  $\sim 1.2 \times 10^5$  laser pulses.

The images in Figure 2 a–f show the characteristic appearance of isolated nanoparticles and the evolution of less-than-one layer deposits with the number of pulses applied on a CdS target at 527 and 263 nm. At both wavelengths it is observed that in this regime the surface density of nanoparticles progressively increases with the number of pulses, while their size seems not to be affected significantly. For the two materials, the application of a higher number of pulses induces the formation of some larger aggregates resulting from the accumulation of isolated nanoparticles arriving nearby at the same substrate location.

The deposited nanoparticles present an oblate shape with the major cross section parallel to the substrate. The average aspect ratio between the in-plane diameter and height is  $\approx 5$  at 527 nm and  $\approx 8$  at 263 nm. The nanoparticle size distribution, in terms of their ESD, was measured in less-than-one layer deposits. As an example, Figure 3 reports the size histograms of CdS nanoparticles deposited at 527 nm (2640 pulses of 440  $\mu$ J) and 263 nm (2640 pulses of 130  $\mu$ J). These experimental conditions

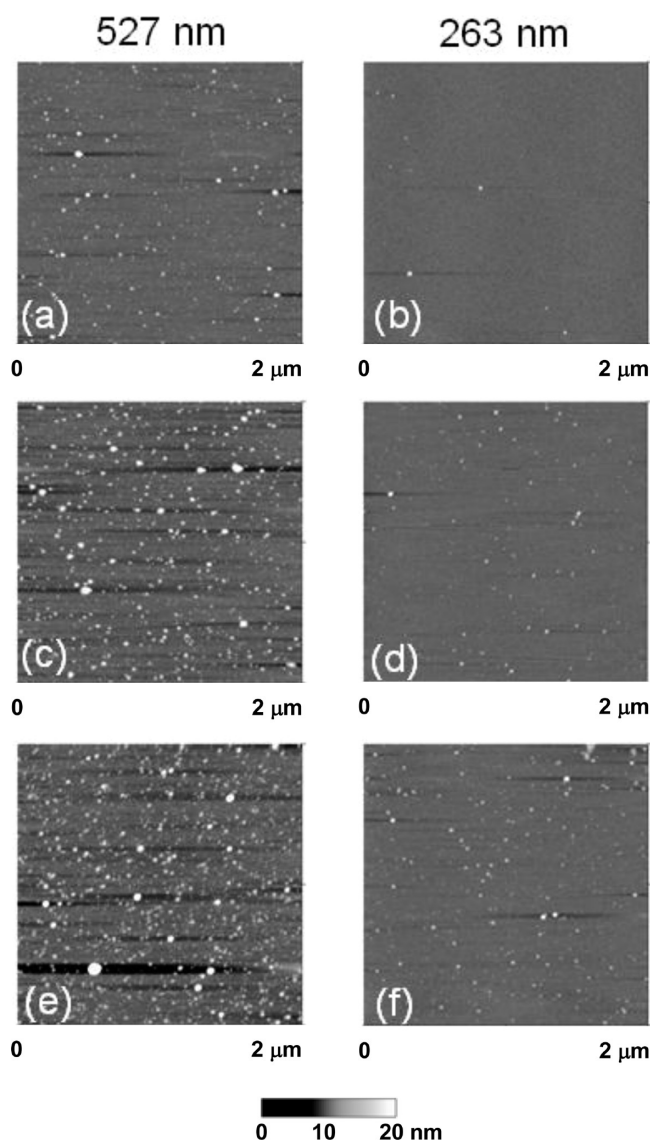


**Figure 2.** AFM images of less-than-one layer CdS deposits on mica made at 527 nm with 440  $\mu$ J per pulse (left) and at 263 nm with 130  $\mu$ J per pulse (right). The number of pulses is 660 (a and b), 2640 (c and d), and 5280 (e and f). The dimensions of each AFM image are  $2 \times 2 \mu\text{m}^2$ . The bar indicates height from 0 to 20 nm.

correspond to five times the fluence threshold for ablation of the CdS target at each wavelength.

It is observed that at 263 nm the nanoparticles are smaller than at 527 nm, at a fluence level which is comparable with respect to the respective ablation threshold. In particular, at 263 nm 90% of the nanoparticles have an ESD below  $\approx 5$  nm, while at 527 nm 90% are counted with an ESD below  $\approx 13$  nm. The same increasing tendency with wavelength holds for the value of the median. Moreover, the total volume of the deposited nanoparticles at 527 nm is about 10 times more than at 263 nm. Even if a lower amount of ablated material is expected at 263 nm due to the reduced laser spot area with respect to 527 nm (a factor of  $\approx 4$ ), this indicates a larger efficiency of ablation for CdS irradiated by ultrashort pulses at visible wavelengths. As it will be shown below, this increasing trend with wavelength is also observed for the thickness of deposits fabricated with a



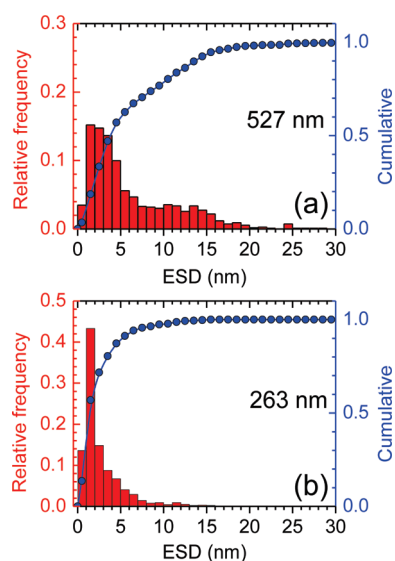


**Figure 3.** Size distribution of the equivalent spherical diameter (ESD) of CdS-deposited nanoparticles grown with 2640 pulses (a) of 440  $\mu\text{J}$  at 527 nm and (b) of 130  $\mu\text{J}$  at 263 nm.

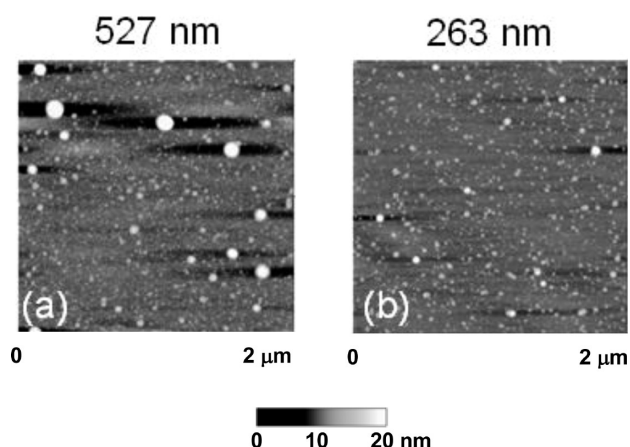


**Figure 4.** Representative AFM images of ZnS deposits: (a) 527 nm, 660 pulses of 440  $\mu\text{J}$ ; (b) 263 nm, 21 120 pulses of 130  $\mu\text{J}$ . The dimensions of each AFM image are  $2 \times 2 \mu\text{m}^2$ . The bar indicates height from 0 to 20 nm.

high number of pulses ( $1.2 \times 10^5$ ) consisting of assembling of nanoparticles.

For comparison Figure 4 shows two representative AFM images of a less-than-one layer ZnS deposit at 527 (660 pulses of 440  $\mu\text{J}$ ) and 263 nm (21 120 pulses of 130  $\mu\text{J}$ ) obtained in experimental conditions where a similar surface density of nanoparticles is achieved. Given the notably different number of laser shots used, we can infer that, also for ZnS, ablation at the visible wavelength is more effective in generating nanoparticles. Moreover, at 527 nm the amount of larger nanoparticles is higher than at 263 nm, thus suggesting that UV ablation of these semiconductors, at a similar fluence level with respect to the ablation threshold, is characterized by a larger atomization and a tendency toward the formation of smaller sized nanoparticles.

AFM images of nanoparticle-assembled films were also acquired. An example is reported in Figure 5, where representative topography, panel a, and phase, panel b, pictures for CdS films

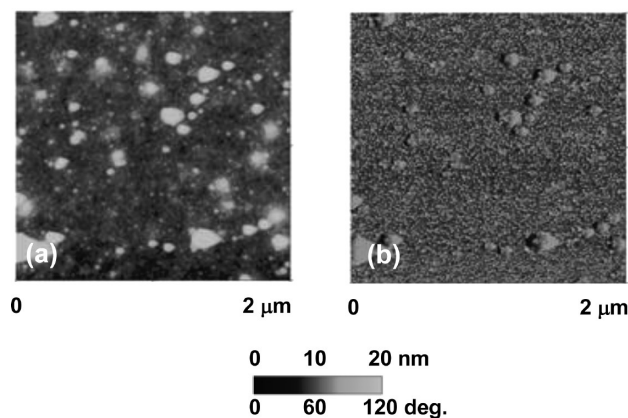


**Figure 5.** AFM image of a nanoparticle-assembled CdS film on Si(100) fabricated at 527 nm with  $1.2 \times 10^5$  laser pulses of 440  $\mu\text{J}$ : (a) topography; (b) phase. The dimensions of each image are  $2 \times 2 \mu\text{m}^2$ . The bar of the left panel indicates height from 0 to 60 nm. The bar of the right panel indicates phase from  $0^\circ$  to  $120^\circ$ .

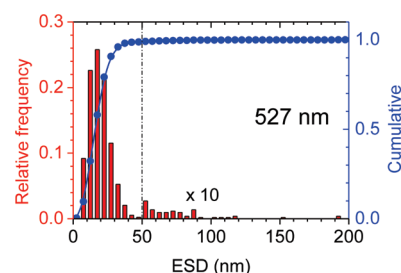


**Figure 6.** Size distribution of the equivalent spherical diameter (ESD) of the nanoaggregates constituting the nanoparticle-assembled CdS film fabricated at 527 nm with  $1.2 \times 10^5$  laser pulses of 440  $\mu\text{J}$  obtained by applying the watershed segmentation method (see, e.g., <http://www.imagemet.com/WebHelp/spip.htm>). Note that the relative frequency of the aggregates larger than 50 nm is augmented 10 times.

deposited at 527 nm are displayed. The AFM images indicate that the film is formed by assembly of the nanoparticles observed in less-than-one layer deposits. The basic structure of the nanoparticle-assembled films is that of a cauliflower-like aggregate of nanoparticles sticking to one another, similarly to what was observed before for metals in similar experimental conditions.<sup>36</sup> From the images we can identify a multitude of small particles whose sizes are comparable to those observed in less-than-one layer deposits, and several regions where the original nanoparticles have stuck on the same area forming larger aggregates. In an attempt to obtain further insight into the size of the nanoparticle-assembled building blocks, the AFM images were analyzed by using an image processing software.<sup>37</sup> While isolated particles are typically analyzed with a classical threshold segmentation method in the case of particles inside aggregated films, a more advanced method, named watershed segmentation, is usually employed.<sup>37</sup> Figure 6 reports the size distribution of the particles present in the film as obtained by this method. We observe that about 90% of the particles in the film are counted with an ESD below  $\approx 30$  nm, thus suggesting that most of the nanoparticles preserve their individuality in the film. Moreover, some larger nanostructures with ESD larger than 50 nm are also detected, which are likely due to aggregation of nanoparticles and whose contribution is somewhat minor.

**Table 1.** Thickness of Deposits (in nm) Grown with  $1.2 \times 10^5$  Laser Pulses, As Measured through AFM<sup>a</sup>

material	527 nm, 440 $\mu$ J	263 nm, 130 $\mu$ J	263 nm, 260 $\mu$ J
CdS	170	20	50
ZnS	75	17	30

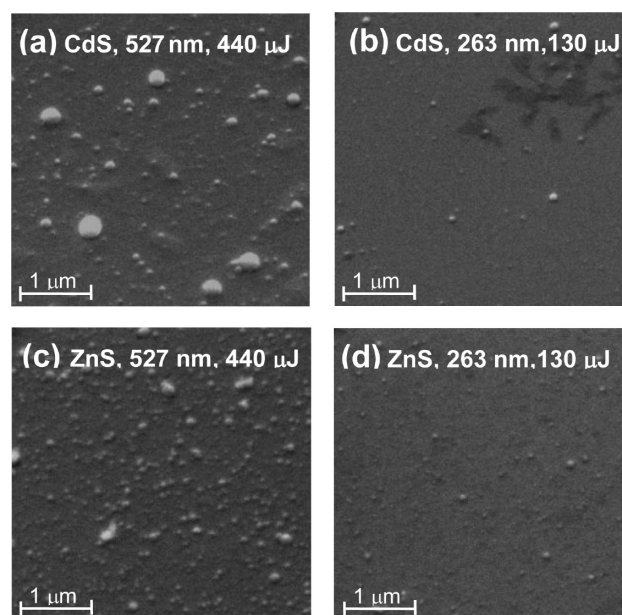
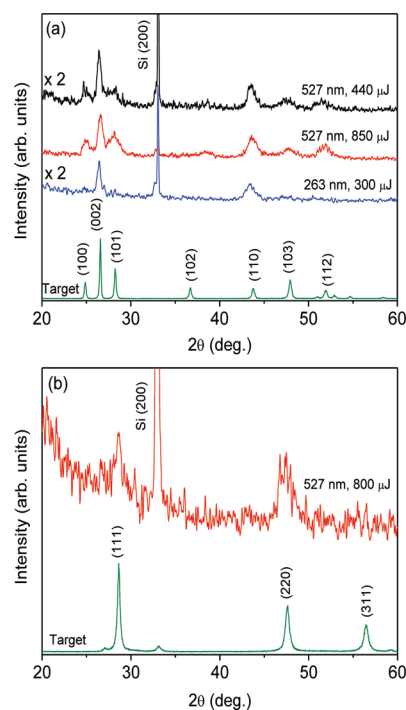
<sup>a</sup> The error is  $\pm 10\%$ .

The thickness of films was also measured by AFM, and the results are summarized in Table 1. While, as expected, higher energy per pulse implies the formation of thicker deposits, it is observed that, at a fluence level which is comparable with respect to the respective ablation threshold, the thickness of deposits is larger upon irradiation in the visible. It is also noticed that deposits grown by irradiating CdS targets are thicker than those made out of ZnS under the same irradiation conditions. These differences are mainly related to differences in the light absorption in the visible and UV wavelengths and the higher effective absorption of CdS as compared with ZnS. CdS and ZnS are direct band gap semiconductors with reported band gap energy of 2.25–2.45 and 3.5–3.8 eV, respectively.<sup>3,38,39</sup> At 527 nm, electronic excitation to the conduction band requires two photons for ZnS, and one photon is nearly enough for CdS. At 263 nm absorption of only one laser photon promotes the electron well above into the conduction band of both semiconductors. At this wavelength, the reported linear absorption coefficients of CdS and ZnS are  $8.0 \times 10^5$  and  $2.4 \times 10^5$  cm<sup>-1</sup>, respectively.<sup>40,41</sup>

We have estimated the ratio of the effective absorption coefficients  $\alpha_{\text{eff}}$  at the two wavelengths based on the dependence of the etching depth  $\delta$  on the incident fluence using the expression<sup>42</sup>  $\delta = 1/\alpha_{\text{eff}} \ln(F/F_{\text{th}})$ . Assuming that the measured thickness of deposits (Table 1) is proportional to the amount of ablated material, we obtain that  $\alpha_{\text{eff}}(263 \text{ nm})/\alpha_{\text{eff}}(527 \text{ nm})$  is 2.5 for CdS and 5 for ZnS.

ESEM analysis was carried out in nanoparticle-assembled films (fabricated with  $1.2 \times 10^5$  pulses). Figure 7 shows representative ESEM pictures of the deposits on Si(100) substrates. When larger aggregates appear, analysis of images indicates that, for CdS, their sizes are in the range of 100–400 at 527 nm and in the range of 80–180 at 263 nm. For ZnS the aggregates are somewhat smaller. The aggregates seen in the ESEM pictures correspond to the larger nanostructures observed by AFM, while the layers of smaller nanoparticles are not completely resolved. The ESEM analysis shows that the diameter of these aggregates tends to increase with wavelength. The superficial density of aggregates in the films grown from the two materials, ranging between 5 and 16  $\mu\text{m}^{-2}$ , also shows an increasing tendency with increasing wavelength. Therefore, generation of higher densities of larger size aggregates is favored at a longer ablation wavelength.

The crystalline quality and composition of the deposits have been characterized using XRD. Figure 8a presents XRD patterns of CdS target material and deposits. For CdS, the XRD peaks of the target sample are located at  $2\theta_{\text{B}}$  ( $\theta_{\text{B}}$  being the Bragg angle) values of 25.1°, 26.6°, 28.2°, 36.6°, 43.9°, 47.9°, and 52.1° and are assigned to (100), (002), (101), (102), (110), (103), and (112) reflections, respectively. This pattern reveals the hexagonal (wurtzite, W) polycrystalline structure of CdS (Joint Committee on Powder Diffraction Standards Card No. 77-2306). Patterns of deposits show a diffraction peak at  $\sim 32^\circ$  which corresponds to Si(200). This peak is assigned to multiple scattering effects in the Si substrate from spots in higher-order Laue zones close to the

**Figure 7.** ESEM images of deposits prepared on Si(100) of CdS by applying  $1.2 \times 10^5$  laser pulses (a) of 440  $\mu$ J at 527 nm and (b) of 130  $\mu$ J at 263, and of ZnS by applying  $1.2 \times 10^5$  laser pulses (c) of 440  $\mu$ J at 527 nm and (d) of 130  $\mu$ J at 263 nm.**Figure 8.** XRD patterns of CdS (a) and ZnS (b) fs PLD nanostructured films grown on Si(100) using  $1.2 \times 10^5$  laser pulses at the indicated conditions. The patterns obtained in the respective targets are also shown.

Ewald sphere.<sup>43</sup> The XRD patterns of deposits fabricated at 527 nm show similar peak distribution as the target. This similarity indicates that the major phase in these samples is hexagonal, although the peaks at 26.6° and 43.9° could also have contribution of the (111) and (220) reflections of the cubic phase

(zincblende, Z). The dominating appearance of the CdS(002) peak would point to a perpendicular orientation of the *c*-axis with respect to the substrate surface, whereas a weak CdS(002) and intense CdS(100) and CdS(110) peaks are signs of a parallel orientation of the *c*-axis. The XRD results show that the material deposited at 527 nm contains a mixture of the two orientations. This can be explained either by a sudden solidification of the material on the substrate, which would prevent the slower growth on a preferential direction, or by the randomly oriented arrival of aggregates to the substrate. The increase of laser fluence results in a variation of the preferential crystal orientation as shown in Figure 8a by the slight relative decrease of intensity of the (002) peak. On the other hand, the more intense and defined peaks obtained in the deposits grown at higher pulse energy can be related to their larger thickness (see Table 1).

Differently from observations at 527 nm, the XRD patterns of deposits fabricated at 263 nm do not coincide with those of the target; in fact, the two peaks, around  $2\theta_B$  values of  $27^\circ$  and  $44^\circ$  assigned to the W(002)/Z(111) and W(110)/Z(220) reflections, are the only ones present in the XRD patterns of deposits grown in the UV, indicating the reduced content of the hexagonal W-phase under these fabrication conditions. As reported elsewhere,<sup>44,45</sup> the hexagonal phase can be found both in the bulk and in nanocrystalline CdS, while the cubic phase is only observed in the nanocrystalline form of this material. Therefore, while the XRD patterns of CdS deposits grown at the visible wavelength are primarily hexagonal wurtzite as the initial target, those grown in the UV appear to display a higher cubic zincblende content.

Figure 8b presents X-ray diffractograms taken on a ZnS target and on a deposit grown at 527 nm using laser pulses of 800  $\mu\text{J}$ . The main XRD peaks, located at  $28.6^\circ$ ,  $47.7^\circ$ , and  $56.4^\circ$ , are assigned to ZnS(111), (220), and (311), respectively. This pattern reveals the predominance of the cubic (sphalerite, S) polycrystalline structure of this material (Joint Committee on Powder Diffraction Standards Card No. 5-566). Upon visible irradiation of ZnS, the XRD patterns obtained upon lower energy per pulse or under UV irradiation (not shown) do not contain any diffraction peak. This is probably due to the reduction of the film thickness at lower fluence and at short irradiation wavelength (Table 1), which deters the possibility of analysis of the crystalline structure of these deposits.

The average crystalline domain size of deposits has been estimated using the Scherrer law,  $D = 0.9 \lambda / B \cos \theta_B$ , where  $\lambda$  is the X-ray wavelength (Cu K $\alpha$  = 0.154 nm) and  $B$  is the full width at half-maximum (in radians) of the diffraction peak. Analysis of W(002)/Z(111) and W(110)/Z(220) peaks of CdS deposits yields a grain size of around 23 and 13 nm, respectively. For these two peaks, the relative increase of width and consequent size reduction follows the trend of the target material, and it has also been observed in CdS nanoparticles produced by chemical procedures.<sup>44</sup> For ZnS, the estimated average crystalline domain size grown at 527 nm is around 7 nm. The XRD analysis seems to indicate that typical crystalline sizes are of the order of the nanoparticle size derived from AFM imaging analysis of the film (see, e.g., Figure 6), thus indicating that the observed nanostructures are likely to be single-crystalline particles.

XPS spectra were recorded in the obtained nanostructured films, and the results are summarized in Table 2. For CdS, all the Cd 3d and all S 2p spectra recorded from the different samples were essentially identical. The binding energy of the Cd 3d<sub>5/2</sub>

**Table 2. Element Ratio in CdS and ZnS Derived from XPS Measurements of Target and Deposits Grown with  $1.2 \times 10^5$  Laser Pulses at the Indicated Conditions<sup>a</sup>**

ratio	target	527 nm, 440 $\mu\text{J}$	527 nm, 800 $\mu\text{J}$	263 nm, 130 $\mu\text{J}$	263 nm, 260 $\mu\text{J}$
Cd/S	1.00	1.00	1.00	0.9	0.9
Zn/S	1.00	1.06	1.00	1.59	1.14

<sup>a</sup> The error is  $\pm 10\%$ .

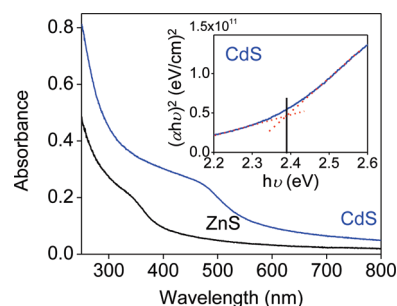


**Figure 9.** Absorbance spectra of CdS and ZnS deposits on glass at 263 nm ( $1.2 \times 10^5$  laser pulses of 130  $\mu\text{J}$ ). The inset shows the Tauc plot of CdS and the estimated band gap value.

and S 2p<sub>3/2</sub> core levels was measured to be  $405.2 \pm 0.2$  and  $161.1 \pm 0.2$  eV, respectively, in all cases. These values are fully compatible with the presence of CdS.<sup>46</sup> Upon irradiation at 527 nm the obtained deposits are stoichiometric, while those grown at 263 nm display a slight excess of S<sup>2-</sup>. For ZnS, the binding energies of the Zn 2p<sub>3/2</sub> and S 2p core levels measured in all the samples (1022.0 and 169.6 eV, respectively) are compatible with the presence of ZnS.<sup>47</sup> For the deposits grown at 527 nm, the S/Zn atomic ratio is 1.0, that is, the expected stoichiometry, while those at 263 nm show an excess of Zn<sup>2+</sup>. Compositional variations with respect to the target have been reported in fs PLD of CdS and other materials<sup>8,9,12,28</sup> and have been attributed to selective evaporation of target components and/or aggregation in the gaseous ablation plume.

The UV–vis absorption spectra of deposits on glass were measured in the 250–800 nm range, and no significant differences were observed between those recorded on deposits grown under visible and UV irradiation. Representative ones, displayed in Figure 9, reveal the high transparency of the deposits for wavelengths longer than the absorption threshold. Tauc plots of  $(\alpha h\nu)^2$ ,  $\alpha$  being the optical absorption coefficient derived from the measured absorbance, as a function of  $h\nu$  serve to estimate the band gaps of deposits<sup>39</sup> (see inset in Figure 9). The determined band gaps are 2.4 eV (CdS) and 3.5 eV (ZnS). These values are not significantly blue-shifted relative to the values of the band gap in bulk hexagonal W-type CdS and cubic S-type ZnS, respectively<sup>3,38,39</sup> because the size of the involved superficial nanostructures of deposits is not small enough for quantum confinement effects to be relevant.

The photoluminescence spectra of CdS and ZnS nanostructured films deposited on Si(100) are shown in Figure 10. Upon excitation at 325 nm, the spectra of CdS deposits grown at 527 nm are constituted by two bands, one sharp around 500 nm and a second broad emission centered at 700 nm. At 263 nm the photoluminescent signal from a deposit grown with the same number of pulses (not shown) is much weaker, although the two



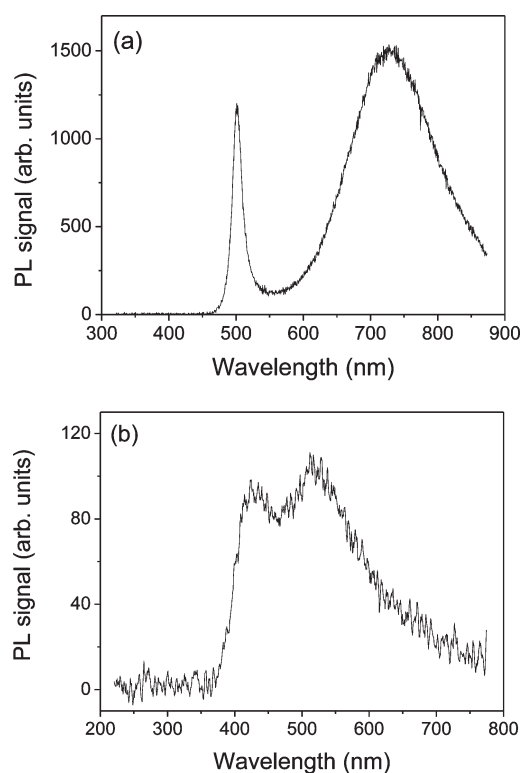


**Figure 10.** Photoluminescence spectra of deposits on Si(100) of (a) CdS at 527 nm ( $1.2 \times 10^5$  laser pulses of 440  $\mu\text{J}$ ) and (b) ZnS at 263 nm ( $1.2 \times 10^5$  laser pulses of 130  $\mu\text{J}$ ).

bands are still present. The lower thickness of the deposit grown at this UV wavelength (Table 1) explains the rather weak signal. For ZnS two bands are also observed centered at 420 and 520 nm. According to previous studies,<sup>19,20,26,48–55</sup> the two bands observed for both materials are attributed to two different decay routes, and their position and width are related with the material composition. In CdS, the sharp, short wavelength band is assigned to the decay of photogenerated charge carriers by radiative recombination at the band edge. The broad, long wavelength band is due to the decay from trap states localized at the surface crystalline defect sites and having energy levels within the forbidden band gap. In ZnS, the band at 420 nm is attributed to transitions from energy levels of sulfur vacancies, and the emission band at 520 nm is produced when electron transit occurs from the energy levels of sulfur vacancies to energy levels of zinc vacancies.<sup>52,53</sup> This assignment is supported by the stoichiometric characterization via XPS as indicated above (see Table 2).

The occurrence of surface-trap states, favored in the case of nanoparticles, is due to the high surface to volume ratio, although it also arises from stoichiometric excess of  $\text{Cd}^{2+}/\text{Zn}^{2+}$  or  $\text{S}^{2-}$ .<sup>45</sup> The disturbed stoichiometry of the deposits, as determined by XPS, can thus be correlated with the position and width of the long wavelength fluorescence band. In fact, the large width of this band suggests a high density of trap states in the forbidden band gap.

As has been shown in this work, ablation of CdS and ZnS solid targets with pulses of 300 fs at the two wavelengths of 527 and 263 nm leads to the deposition of isolated nanoparticles and, at sufficiently high number of pulses, to the formation of thin nanostructured films constituted by the assembly of individual

crystalline nanoparticles. The laser wavelength has a noticeable effect on the velocity of atomic plume species, on the size of the nanoparticles, and on the crystalline structure and stoichiometry of the deposited films. The size of isolated nanoparticles increases with wavelength, a tendency already observed for CdS and other semiconductor materials with pulses of 60 fs from a Ti:sapphire laser.<sup>8,9,17</sup> While at 527 nm the deposits maintain the crystalline phase of the target (hexagonal in the case of CdS and cubic for ZnS) and are stoichiometric, at 263 nm significant differences are noticed.

The results shown herein were obtained by comparing two laser wavelengths at fluences about five times the respective ablation threshold and under focusing conditions corresponding to a spot area which is four times larger under visible irradiation. Previous works<sup>7,12</sup> have discussed the important role of the laser spot size in fs ablation and the effect on the morphology and structure on deposits. It has also been shown that changes in the laser spot size would affect the angular distribution of the atomic and cluster fraction in the plume thus influencing the composition of deposits and their thickness in the direction normal to the target. In particular, it has been reported<sup>7</sup> that high fluences and large spot size favor the ejection of nanoparticles and droplets with respect to the emission of atomic species. In our case, ablation under tight focusing conditions results in an emitting plume with similar composition and expansion velocities at both wavelengths. This, together with the low intensity of emission from nanoparticles and the absence of luminous clusters in the plume, indicates that the effect of laser spot size on the plume composition should be minimal. Also in ref 7 it was shown that the ratio between the initial radial and axial dimensions of the plasma ( $\sigma = Z/R$ ) is an important parameter which characterizes the initial pressure gradient and governs the plasma expansion.

More recently, some of the authors have shown<sup>56</sup> that the angular distribution of the plumes and the thickness profile of the deposits produced during ultrafast laser ablation of a solid target are well described by the Anisimov model.<sup>57</sup> The Anisimov model provides a gas dynamical description of the adiabatic phase of expansion of a gas cloud in a vacuum, and it has been successfully applied to PLD with nanosecond laser pulses. In particular, also in this model the ratio between the initial radial and axial dimensions of the expanding plume,  $\sigma$ , is a fundamental parameter in defining the characteristics of the plume expansion and the thickness profile of the deposits, in agreement with the description given in ref 7. In particular, in ref 56 it was observed that the thickness profile of the deposited films is consistent with an Anisimov-type expansion of a layer characterized by a radial dimension equal to the radius of the laser beam spot and an axial dimension roughly equal to a few times the ablation depth. Therefore, assuming that the initial axial dimension is of the order of the thickness of the ablated volume of the target, which for ultrashort pulse durations is approximated by the absorption depth or  $\alpha_{\text{eff}}^{-1}$ , and that the radial dimension is the radius of the laser beam spot, we can estimate the value of  $\sigma$  in the two spectral regimes of irradiation. Using the reported ratio of effective absorption coefficients and considering the different spot sizes, we can conclude that similar  $\sigma$  values characterize the plume expansion and thickness profile in the visible and UV. Thus, although the influence of laser spot size cannot be totally neglected, it can be assumed to exert a minimal influence in the composition and dynamics of the plume of the semiconductor materials considered herein under the present experimental conditions.



The observed tendencies can thus be discussed in reference to the initial ablation step, the plasma kinetic energy, and the aggregation processes happening on the substrate surface. Under irradiation, laser light is coupled to a superficial skin layer of the target (approximated by the value of  $\alpha_{\text{eff}}^{-1}$ ) which experiences an intense heating. As the heat diffusion time, estimated at around 10 ps,<sup>9</sup> fully exceeds the laser pulse duration, electron–lattice thermal equilibrium is not reached within this time interval, and the material remains confined without expansion while the pulse lasts. Once energy deposition by the pulse is completed, this isochoric transition in the phase diagram is followed by adiabatic expansion and decomposition of the created plasma from an initially high temperature.<sup>7,9,14,15</sup> As discussed, the coupling of laser energy to the semiconductor target material takes place by different absorption processes according to the wavelength. Under UV irradiation, the coupling is mediated by one-photon absorption process in a thin layer below the exposed surface. In the visible, due to the higher order of the multiphoton processes involved (at least two-photon for ZnS), the value of  $\alpha_{\text{eff}}$  is lower than in the UV (by 2.5 times in CdS and by 5 times in ZnS according to our estimation). This implies that the visible deeper regions below the surface are thermally affected by irradiation.

In thermodynamic analysis models,<sup>14,15</sup> the properties of the ejecta in fs ablation plumes are related to the depth with respect to the target surface from where the material is originated, as this depth determines the trajectory followed in the phase diagram. Under UV irradiation, due to the thin skin depth, the material is exposed to an intense heating that decomposes the solid by exceeding its cohesion energy and results in complete vaporization. Upon visible irradiation due to the lower effective absorption coefficient, the favored phase explosion and fragmentation mechanisms lead to an inhomogeneous mixture of larger size fragments. As a consequence, the characteristic size trend reflects the different trajectories followed by the expanding plasma following the initial excitation at the two wavelengths.

In fact, previous TOF-MS work by some of the authors<sup>58</sup> had investigated the cationic content of CdS ablation plumes in a nanosecond laser experiment at a range of wavelengths from the UV to the IR (the fundamental, second, third, and fourth harmonics of a Nd:YAG laser). A clear difference was observed between 266 nm irradiation and the longer wavelengths. Whereas for the latter the plume exhibited a considerable proportion of aggregates and clusters (groups  $(\text{CdS})_2$  to  $(\text{CdS})_{34}$  were observed), at 266 nm irradiation this so-called “heavy” family represented an extremely low proportion of the mass spectra, with atomic species clearly dominating the overall signal. The extension to the situation described in this paper is not straightforward, since the TOF-MS experiment was only sensitive to species in ionized form, and the results correspond to nanosecond irradiation. Nevertheless, it does support the idea that 266 nm ablation produces plumes of an extremely atomized nature, as opposed to longer wavelengths, where larger mass species can be ejected from the target.

With regard to the processes occurring on the substrate, the kinetic energy and flux of plasma species affect the nucleation processes taking place on its surface and consequently have an effect on the crystallinity, stoichiometry, and electronic structure of the nanoparticle-assembled deposits. As already indicated, atomic species resulting from UV ablation of the targets impinge on the substrate with higher kinetic energies. This leads to higher energy of mobility and diffusion of the species on the forming

deposit and, with similarity to observations gathered from studies of fs PLD of CdS and other materials,<sup>11,26,27</sup> allows the orientation in new crystalline conformations and stoichiometries, different from those of the original target material

## 4. CONCLUSIONS

In conclusion, isolated nanoparticles and nanoparticle-assembled films of the wide band gap II–VI semiconductors CdS and ZnS were fabricated by pulsed laser deposition at the wavelengths of 527 and 263 nm from a Nd:Glass laser with pulses of  $\approx 300$  fs. The nanoparticle size scales with wavelength; UV and visible ablation yield nanoparticles of 5 and 13 nm average diameter, respectively, in the case of CdS and somewhat larger for ZnS. The films obtained are highly transparent and photoluminescent under UV excitation. It is observed than in the UV, the crystalline phase and stoichiometry of the films markedly differ from those of the targets while in the visible the deposits keep their structural and chemical characteristics. The observed trends are discussed in reference to the light absorption step, the plasma dynamics, and the nucleation processes on the substrate using the framework of thermodynamic analysis models. Under UV irradiation, due to the thin affected depth below the surface of the target, vaporization of the plasma is favored. In the visible, due to the lower effective absorption coefficient, phase explosion and fragmentation lead to an inhomogeneous mixture of larger size fragments. The more atomized nature of the UV ablation plume is responsible for the smaller size of both nanoparticles and aggregates and the loss of memory of the initial target structural and chemical characteristics in the deposits.

## AUTHOR INFORMATION

### Corresponding Author

\*E-mail: marta.castillejo@iqfr.csic.es.

## ACKNOWLEDGMENT

Funding has been provided by Ministry of Science and Innovation of Spain (MICINN) Project CTQ2007-60177. M.S. thanks CAM (Geomateriales P2009/MAT 1629) for a contract. Dr. E. Rebollar is acknowledged for help with determination of AFM thicknesses.

## REFERENCES

- (1) Nanda, J.; Sapra, S.; Sarma, D. D.; Chandrasekharan, N.; Hodes, G. *Chem. Mater.* **2000**, *12*, 1018.
- (2) Chen, X.; Mao, S. S. *Chem. Rev.* **2007**, *107*, 2891.
- (3) Hullavarad, N. V.; Hullavarad, S. S.; Karulkar, P. C. *J. Nanosci. Nanotechnol.* **2008**, *8*, 3272.
- (4) Ma, C.; Moore, D. F.; Li, J.; Wang, C. L. *Adv. Mater.* **2003**, *15*, 228.
- (5) Amoroso, S.; Ausanio, G.; Bruzzese, R.; Vitiello, M.; Wang, X. *Phys. Rev. B* **2005**, *71*, 033406.
- (6) Zhang, Y.; Russo, R. E.; Mao, S. S. *Appl. Phys. Lett.* **2005**, *87*, 133115.
- (7) Perrière, J.; Boulmer-Leborgne, C.; Benzerga, R.; Tricot, S. *J. Phys. D: Appl. Phys.* **2007**, *40*, 7069.
- (8) Sanz, M.; Walczak, M.; de Nalda, R.; Oujja, M.; Marco, J. F.; Rodríguez, J.; Izquierdo, J. G.; Bañares, L.; Castillejo, M. *Appl. Surf. Sci.* **2009**, *255*, 5206.
- (9) Sanz, M.; de Nalda, R.; Marco, J. F.; Izquierdo, J. G.; Bañares, L.; Castillejo, M. *J. Phys. Chem. C* **2010**, *114*, 4864.
- (10) Okoshi, M.; Higashikawa, K.; Hanabusa, M. *Jpn. J. Appl. Phys.* **2001**, *40*, 1287.

- (11) Perrière, J.; Millon, E.; Seiler, W.; Boulmer-Leborgne, C.; Craciun, V.; Albert, O.; Loulergue, J. C.; Etchepare, J. J. *Appl. Phys.* **2002**, *91*, 690.
- (12) Millon, E.; Perrière, J.; Défourneau, R. M.; Défourneau, D.; Albert, O.; Etchepare, J. *Appl. Phys. A: Mater. Sci. Process.* **2003**, *77*, 73.
- (13) Henley, S. J.; Fuge, G. M.; Ashfold, M. N. R. *J. Appl. Phys.* **2005**, *97*, 023304.
- (14) Eliezer, S.; Eliaz, N.; Grossman, E.; Fisher, D.; Gouzman, I.; Henis, Z.; Pecker, S.; Horovitz, Y.; Fraenkel, M.; Maman, S.; Lereah, Y. *Phys. Rev. B* **2004**, *69*, 144119.
- (15) Lewis, L. J.; Perez, D. *Appl. Surf. Sci.* **2009**, *255*, 5101.
- (16) Amoruso, S.; Bruzzese, R.; Spinelli, N.; Velotta, R.; Vitiello, M.; Wang, X.; Ausanio, G.; Iannotti, V.; Lanotte, L. *Appl. Phys. Lett.* **2004**, *84*, 4502.
- (17) Gámez, F.; Plaza-Reyes, A.; Hurtado, P.; Guillén, E.; Anta, J. A.; Martínez-Haya, B.; Pérez, S.; Sanz, M.; Castillejo, M.; Izquierdo, J. G.; Bañares, L. *J. Phys. Chem. C* **2010**, *114*, 17409.
- (18) Zhai, T.; Fang, X.; Li, L.; Bando, Y.; Golberg, D. *Nanoscale* **2010**, *2*, 168.
- (19) Zhu, Y.; Shen, Z. X.; Lim, Y. V.; Zang, H.; Liu, Y.; Wee, A. T. S. *J. Phys.: Conf. Ser.* **2006**, *28*, 127.
- (20) Nanda, J.; Sarma, D. D. *J. Appl. Phys.* **2001**, *90*, 2504.
- (21) Ullrich, B.; Sakai, H.; Segawa, Y. *Thin Solid Films* **2001**, *385*, 220.
- (22) Perna, G.; Capozzi, V.; Ambrico, M.; Augelli, V.; Lingonzo, T.; Minafra, A.; Schiavulli, L.; Pallara, M. *Thin Solid Films* **2004**, *187*, 453.
- (23) Mahdavi, S. M.; Irajizad, A.; Tilaki, R. M. *Opt. Mater.* **2005**, *27*, 1583.
- (24) Vigil-Galán, O.; Vidal-Larramendi, J.; Escamilla-Esquivel, A.; Contreras-Puente, G.; Cruz-Gandarilla, F.; Arriaga-Mejía, G.; Chavarria-Castañeda, M.; Tufiño-Velázquez, M. *Phys. Status Solidi* **2006**, *203*, 2018.
- (25) Acharya, K. P.; Skuza, J. R.; Lukaszew, R. A.; Liyanage, C.; Ullrich, B. *J. Phys.: Condens. Matter* **2007**, *19*, 196221.
- (26) Tong, X. L.; Jiang, D. S.; Liu, L.; Liu, Z. M.; Luo, M. Z. *Opt. Commun.* **2007**, *270*, 356.
- (27) Tong, X. L.; Jiang, D. S.; Li, Y.; Liu, Z. M.; Luo, M. Z. *Physica B* **2006**, *382*, 105.
- (28) Tong, X. L.; Jiang, D. S.; Liu, Z. M.; Luo, M. Z.; Li, Y.; Lu, P. X.; Yang, G.; Long, H. *Thin Solid Films* **2008**, *516*, 2003.
- (29) McLaughlin, M.; Sakeek, H. F.; Maguire, P.; Graham, W. G.; Molloy, J.; Morrow, T.; Laverty, S.; Anderson, J. *Appl. Phys. Lett.* **1993**, *63*, 1865.
- (30) Shen, W. P.; Kwok, H. S. *Appl. Phys. Lett.* **1994**, *65*, 2162.
- (31) Hiramatsu, H.; Ohta, H.; Hirano, M.; Hosono, H. *Solid State Commun.* **2002**, *124*, 411.
- (32) Sanz, M.; Castillejo, M.; Amoruso, S.; Ausanio, G.; Bruzzese, R.; Wang, X. *Appl. Phys. A: Mater. Sci. Process.* **2010**, *101*, 639.
- (33) Wagner, C. D.; Davis, L. E.; Zeller, M. V.; Taylor, J. A.; Raymond, R. M.; Gale, L. H. *Surf. Interface Anal.* **1981**, *3*, 211.
- (34) Grojo, D.; Hermann, J.; Perrone, A. *J. Appl. Phys.* **2005**, *97*, 063306.
- (35) Amoruso, S.; Bruzzese, R.; Pagano, C.; Wang, X. *Appl. Phys. A: Mater. Sci. Process.* **2007**, *89*, 1017.
- (36) Amoruso, S.; Ausanio, G.; Bruzzese, R.; Lanotte, L.; Scardi, P.; Vitiello, M.; Wang, X. *J. Phys.: Condens. Matter* **2006**, *18*, L49.
- (37) SPIP<sup>TM</sup>, Image Metrology; see <http://www.imagemet.com/WebHelp/spip.htm>.
- (38) Berger, L. I.; Pamplin, B. P. Properties of semiconductors. In *Handbook of Chemistry and Physics*, 73rd ed.; Weast, R. C., Ed.; CRC Press: Boca Raton, FL, 1993.
- (39) Bakke, J. R.; Jung, H. J.; Tanskanen, T.; Sonclair, R.; Bent, S. F. *Chem. Mater.* **2010**, *22*, 4669.
- (40) *Handbook of Optical Constants of Solids*; Palik, E. D., Ed.; Academic Press: New York, 1997.
- (41) Leung, K. M.; Tang, C. C.; Deshazer, L. G. *Thin Solid Film* **1976**, *34*, 119.
- (42) Srinivasan, R.; Braren, B. *Chem. Rev.* **1989**, *89*, 1303.
- (43) Tu, K. N.; Howie, A. *Philos. Mag. B* **1978**, *37*, 73.
- (44) Banerjee, R.; Jayakrishnan, R.; Ayyub, P. *J. Phys.: Condens. Matter* **2000**, *12*, 10647.
- (45) Singh, V.; Sharma, P. K.; Cahuhan, P. *Mater. Chem. Phys.* **2010**, *121*, 202.
- (46) Marychurch, M.; Morris, G. C. *Surf. Sci.* **1985**, *154*, L251.
- (47) Xu, J. F.; Ji, W.; Lin, J. Y.; Tang, S. H.; Du, Y. W. *Appl. Phys. A: Mater. Sci. Process.* **1998**, *66*, 639.
- (48) Sun, H.; Mu, J. *J. Disp. Sci. Technol.* **2005**, *26*, 719.
- (49) Mandal, D.; Hosoi, H.; Chatterjee, U.; Tahara, T. *J. Chem. Phys.* **2009**, *130*, 034902.
- (50) Orii, T.; Kaito, S.; Matsuishi, K.; Onari, S.; Arai, T. *J. Phys.: Condens. Matter* **2002**, *14*, 9743.
- (51) Higuchi, S.; Hanabusa, M. *Appl. Surf. Sci.* **2000**, *154–155*, 238.
- (52) Lu, H. Y.; Chu, S. Y.; Tan, S. S. *J. Cryst. Growth* **2004**, *269*, 385.
- (53) Yoo, Y. Z.; Osaka, Y.; Fukumura, T.; Zhengwu, J.; Kawasaki, M.; Koinuma, H.; Chikyow, T.; Ahmet, P.; Setoguchi, A.; Chichibu, S. F. *Appl. Phys. Lett.* **2001**, *78*, 616.
- (54) Arul Dhas, N.; Zaban, A.; Gedanken, A. *Chem. Mater.* **1999**, *11*, 806.
- (55) Hiramatsu, H.; Ohta, H.; Hirano, M.; Hosono, H. *Solid State Commun.* **2002**, *124*, 411.
- (56) Donnelly, T.; Lunney, J. G.; Amoruso, S.; Bruzzese, R.; Wang, X.; Ni, X. *J. Appl. Phys.* **2010**, *108*, 043309.
- (57) Anisimov, S. I.; Bauerle, D.; Luk'yanchuk, B. S. *Phys. Rev. B* **1993**, *48*, 12076.
- (58) Álvarez-Ruiz, J.; López-Arias, M.; de Nalda, R.; Martín, M.; Arregui, A.; Bañares, L. *Appl. Phys. A: Mater. Sci. Process.* **2009**, *95*, 681.